

Gut microbiome dysbiosis during COVID-19 is associated with increased risk for bacteremia and microbial translocation.

Mericien Venzon

NYU Grossman School of Medicine

Lucie Bernard-Raichon

NYU Grossman School of Medicine

Jon Klein

Yale University <https://orcid.org/0000-0002-3552-7684>

Jordan Axelrad

NYU Grossman School of Medicine <https://orcid.org/0000-0003-1951-7790>

Grant Hussey

NYU Grossman School of Medicine

Alexis Sullivan

NYU Grossman School of Medicine

Arnau Casanovas-Massana

Yale University <https://orcid.org/0000-0002-3301-6143>

Maria Noval

New York University Grossman School of Medicine

Ana Valero-Jimenez

New York University Grossman School of Medicine

Juan Gago

NYU Grossman School of Medicine

Evan Wilder

NYU Langone Health

Yale IMPACT Research Team

Yale New Haven Health

Akiko Iwasaki

Yale University <https://orcid.org/0000-0002-7824-9856>

Lorna Thorpe

NYU Grossman School of Medicine

Dan Littman

NYU Grossman School of Medicine

Meike Dittmann

New York University Grossman School of Medicine

Kenneth Stapleford

NYU Grossman School of Medicine

Bo Shopsin

Division of Infectious Diseases, Department of Medicine, New York University School of Medicine, NYU Langone Health

Victor Torres

New York University Grossman School of Medicine <https://orcid.org/0000-0002-7126-0489>

Albert Ko

Yale School of Public Health <https://orcid.org/0000-0001-9023-2339>

Ken Cadwell

NYU Grossman School of Medicine

Jonas Schluter (✉ jonas.schluter@nyulangone.org)

NYU Langone Health <https://orcid.org/0000-0002-6214-9367>

Letter

Keywords: microbes, COVID-19, secondary infections, gut microbiome

Posted Date: July 27th, 2021

DOI: <https://doi.org/10.21203/rs.3.rs-726620/v1>

License:  This work is licensed under a Creative Commons Attribution 4.0 International License.

[Read Full License](#)

Version of Record: A version of this preprint was published at Nature Communications on November 1st, 2022. See the published version at <https://doi.org/10.1038/s41467-022-33395-6>.

1 **Gut microbiome dysbiosis during COVID-19 is associated with increased risk for bacteremia and**
2 **microbial translocation.**

3
4 Mericien Venzon^{*1,2}, Lucie Bernard-Raichon^{*2}, Jon Klein^{*3}, Jordan E. Axelrad^{*4}, Grant A. Hussey⁵, Alexis P.
5 Sullivan⁵, Arnau Casanovas-Massana⁶, Maria G. Noval⁷, Ana M. Valero-Jimenez⁷, Juan Gago^{1,8}, Evan
6 Wilder⁴, Yale IMPACT Research Team¹¹, Lorna E. Thorpe⁸, Dan R. Littman^{2,9}, Meike Dittmann⁷, Kenneth
7 A. Stapleford⁷, Bo Shopsisin¹⁰, Victor J. Torres⁷, Albert I. Ko⁶, Akiko Iwasaki^{3,9}, Ken Cadwell^{2,4,7}†, Jonas
8 Schluter^{5,7}†

- 9
10 1. Vilcek Institute of Graduate Biomedical Sciences, New York University Grossman School of
11 Medicine, New York, NY, USA
12 2. Kimmel Center for Biology and Medicine at the Skirball Institute, New York University Grossman
13 School of Medicine, New York, NY, USA
14 3. Department of Immunobiology, Yale University School of Medicine, New Haven, CT, USA
15 4. Division of Gastroenterology, Department of Medicine, New York University Grossman School of
16 Medicine, New York, NY, USA
17 5. Institute for Computational Medicine, New York University Grossman School of Medicine, New York,
18 NY, USA
19 6. Department of Epidemiology of Microbial Diseases, Yale School of Public Health, New Haven, CT,
20 USA.
21 7. Department of Microbiology, New York University Grossman School of Medicine, New York, NY,
22 USA
23 8. Department of Population Health, New York University Grossman School of Medicine, New York,
24 NY, USA.
25 9. Howard Hughes Medical Institute, Chevy Chase, MD.
26 10. Department of Medicine, Division of Infectious Diseases, New York University Grossman School
27 of Medicine, New York, NY, USA
28 11. IMPACT team members listed in the appendix.

29 *) These authors contributed equally

30
31 **Correspondence:**

32 † ken.cadwell@nyulangone.org

33 † jonas.schluter@nyulangone.org

34

35 **Abstract**

36 The microbial populations in the gut microbiome have recently been associated with COVID-19 disease
37 severity. However, a causal impact of the gut microbiome on COVID-19 patient health has not been
38 established. Here we provide evidence that gut microbiome dysbiosis is associated with translocation of
39 bacteria into the blood during COVID-19, causing life-threatening secondary infections. Antibiotics and
40 other treatments during COVID-19 can potentially confound microbiome associations. We therefore first
41 demonstrate that the gut microbiome is directly affected by SARS-CoV-2 infection in a dose-dependent
42 manner in a mouse model, causally linking viral infection and gut microbiome dysbiosis. Comparison with
43 stool samples collected from 101 COVID-19 patients at two different clinical sites also revealed
44 substantial gut microbiome dysbiosis, paralleling our observations in the animal model. Specifically, we
45 observed blooms of opportunistic pathogenic bacterial genera known to include antimicrobial-resistant
46 species in hospitalized COVID-19 patients. Analysis of blood culture results testing for secondary
47 microbial bloodstream infections with paired microbiome data obtained from these patients suggest that
48 bacteria translocate from the gut into the systemic circulation of COVID-19 patients. These results are
49 consistent with a direct role for gut microbiome dysbiosis in enabling dangerous secondary infections
50 during COVID-19.

51 **Main text**

52 A better understanding of factors contributing to the pathology of coronavirus disease 2019 (COVID-19) is
53 an urgent global priority. Infections by SARS-CoV-2 are frequently asymptomatic or mild in nature, but
54 may also cause a broad range of severe and life-threatening symptoms. Previous reports have
55 demonstrated that severe COVID-19 is frequently associated with specific inflammatory immune
56 phenotypes, lymphopenia, and a generally disproportionate immune response leading to systemic organ
57 failure^{1,2}. Even in mild cases, gastrointestinal symptoms are reported frequently, and recent studies
58 reported that COVID-19 patients lose commensal taxa of the gut microbiome during hospitalization^{3,4}.
59 Differences in gut bacterial populations relative to healthy controls were observed in all COVID-19
60 patients, but most strongly in patients who were treated with antibiotics during their hospitalization⁴. Most
61 recently, COVID-19 patients treated with broad spectrum antibiotics at admission were shown to have
62 increased susceptibility to multi-drug resistant infections and nearly double the mortality rate from septic
63 shock^{5,6}, and a recent meta-analysis found that over 14% of 3,338 COVID-19 patients acquired a
64 secondary bacterial infection⁷. However, the causal direction of the relationship between disease
65 symptoms and gut bacterial populations is not yet clear.

66 Complex gut microbiota ecosystems can prevent the invasion of potentially pathogenic
67 bacteria^{8,9}. Conversely, when the gut microbiota incurs damage, such as through antibiotics treatment,
68 competitive exclusion of pathogens is weakened¹⁰ and potentially dangerous blooms of antibiotic resistant
69 bacterial strains can occur^{11,12}. In immunocompromised cancer patients, blooms of Enterococcaceae and
70 Gram-negative proteobacteria can lead to gut dominations by few or single species¹³⁻¹⁶. Gut domination
71 events are dangerous to these patients because antibiotic resistant bacteria may translocate from the gut
72 into the blood stream. Consequently, enterococcal dominations have been associated with 9-fold
73 increased risk of bloodstream infections (BSIs) with vancomycin-resistant Enterococcus (VRE), and
74 domination by Gram-negative proteobacteria with 5-fold increased risk of Gram-negative rod BSIs¹³.
75 Bacterial co-infection can also cause life-threatening complications in patients with severe viral
76 infections^{6,17}; therefore, antibacterial agents were administered empirically to nearly all critically ill
77 suspected COVID-19 patients since the incidence of bacterial superinfection was unknown early during
78 the pandemic^{4,18}. However, it is now known that nosocomial infection during prolonged hospitalization is
79 the primary threat to patients with COVID-19¹⁹, rather than bacterial co-infection upon hospital
80 admission^{7,20-22}. Evidence from immunocompromised cancer patients suggests that indiscriminate
81 administration of broad-spectrum antibiotics may, counter-intuitively, increase nosocomial BSI rates by
82 causing gut dominations of resistant microbes that can translocate into the blood^{13,23}. Thus, empiric
83 antimicrobial use, i.e. without direct evidence for a bacterial infection, in patients with severe COVID-19
84 may be especially pernicious because it may select for antimicrobial resistance and could promote gut
85 translocation-associated BSI.

86

87 The role of the gut microbiome in respiratory viral infections in general²⁴, and in COVID-19
88 patients in particular, is only beginning to be understood. Animal models of influenza virus infection have
89 uncovered mechanisms by which the microbiome influences antiviral immunity²⁵⁻²⁷, and in turn, the viral
90 infection was shown to disrupt the intestinal barrier of mice by damaging the gut microbiota^{28,29}. Hence,
91 we hypothesized that gut dysbiosis during COVID-19 may be associated with BSIs. To test this, we first
92 determined whether SARS-CoV-2 infection could directly cause gut dysbiosis independently of
93 hospitalization and treatment. Daily changes in fecal bacterial populations were monitored following
94 intranasal inoculation of transgenic mice expressing human *ACE2* driven by the *cytokeratin-18* promoter
95 (*K18-ACE2tg* mice) with either a high dose (HD, 10⁴PFU) or low dose (LD, 10PFU) of SARS-CoV-2
96 (**Figure 1a**). Although disease was not as evident in LD mice, we confirmed the presence of infectious
97 virus in the lung by plaque assay at sacrifice (**Supplementary Figure S1**). Among the HD mice, we
98 observed significant microbiome changes (**Figure 1b**), with a repeatedly observed community trajectory
99 corresponding to a loss in relative abundances of obligate anaerobe species such as members of the
100 Clostridiales order (**Figure 1c**), concurrent with an expansion of Verrucomicrobiales (**Figure 1a,c**). During
101 this shift in the microbiome, α -diversity in the gut bacterial ecosystem was decreasing, a trend also
102 observed in the LD mice, albeit to a lesser extent, but not in the control mice (**Figure 1b**). After less than
103 one week of viral infection, α -diversity was reduced in infected mice (**Figure 1b**, 95%HDI<0 Bayesian
104 estimation of differences in group means BEST, methods). Alongside the progressive increase in
105 microbiota compositional dysbiosis, we also observed systemic signs of severe infection, including weight
106 loss (**Supplementary Figure S2**), as well as ruffled fur, heavy breathing, reduced activity and hunched
107 posture (**Supplementary Table S1**). These results demonstrate that SARS-CoV2 infection directly
108 causes gut microbiome dysbiosis in a mouse model.

109 We next profiled the bacterial composition of the fecal microbiome in 138 samples (**Figure 2a**)
110 obtained from SARS-CoV-2 infected patients treated at NYU Langone Health (NYU, 73 samples,
111 **Supplementary Table S2**) and Yale New Haven Hospital (YALE, 65 samples, **Supplementary Table**
112 **S3**). Analysis of metagenomic data obtained from sequencing of the 16S rRNA genes revealed a wide
113 range of bacterial community diversities, as measured by the inverse Simpson index, in samples from
114 both centers (NYU: [1.0, 32.2], YALE: [1.5, 29.3], **Figure 2b**); on average, samples from NYU were less
115 diverse (-2.5, $p < 0.01$, **Figure 2c**). However, the composition in samples between the two centers did not
116 show systematic compositional differences (**Figure 2d,e,f**). On average, in both centers, members of the
117 phyla Firmicutes and Bacteroidetes represented the most abundant bacteria, followed by Proteobacteria
118 (**Figure 2d**). The wide range of bacterial diversities was reflected in the high variability of bacterial
119 compositions across samples (**Figure 2e,f**). In samples from both centers, microbiome dominations,
120 defined as a community where a single genus reached more than 50% of the population, were observed
121 frequently (NYU: 21 samples, YALE: 12 samples), representing states of severe microbiome injury in
122 COVID-19 patients (**Figure 2g**).

123 In agreement with a recent study associating gut microbial compositions with disease severity⁴,
124 we found that samples from patients who were treated in the ICU had reduced bacterial diversity
125 (**Supplementary Figure S3**). In 22 cases, gastrointestinal symptoms were recorded, but only two of
126 those patients required ICU treatment and corresponding stool samples had higher average diversity than
127 other samples (**Supplementary Figure S3**). Strikingly, however, samples associated with a BSI had
128 strongly reduced bacterial α -diversities (mean difference: -7.7, CI_{BEST}[-10.2, -5.2], **Supplementary Figure**
129 **S3**).

130 The lower diversity associated with samples from 21 patients with BSIs led us to investigate their
131 bacterial taxon compositions and the potential that gut dysbiosis was associated with BSI events. All BSI
132 patients had received antibiotic treatments during hospitalization, which could exacerbate COVID-19
133 induced shifts in microbiota populations^{11,12,15}, but may indeed be administered in response to a
134 suspected or confirmed BSI. However, we noted that most BSI patients (80%) also received antibiotics
135 prior to their BSI. Principal coordinate analysis of all stool samples indicated that the BSI-associated
136 samples spanned a broad range of compositions (**Figure 3a**). To identify bacterial abundance patterns
137 that consistently distinguished BSI from non-BSI-associated samples, we next performed a Bayesian
138 logistic regression. This analysis estimated the association of the 10 most abundant bacterial genera with
139 BSI cases, i.e. it identified enrichment or depletion of bacterial genera in BSI associated samples
140 (**Figure 3b**). This analysis revealed that the genus *Faecalibacterium* was negatively associated with BSI
141 (OR: -1.49, CI: [-2.82, -0.18]). *Faecalibacterium* is an immunosupportive Clostridiales genus that is a
142 prominent member of the human gut microbiome³⁰⁻³², and its reduction is associated with disruption to
143 intestinal barrier function^{33,34}, perhaps via ecological network effects³⁴.

144 To evaluate the effect size of the association between *Faecalibacterium* and BSIs, we performed
145 a posterior predictive check. Using the average genus composition found across all samples, we first
146 computed the distribution of predicted BSI risks (**Figure 3c**), and compared this risk distribution with a
147 hypothetical bacterial composition which increased *Faecalibacterium* by 10% points. The predicted risk
148 distributions associated with these two compositions differed strongly (mean difference 26%,
149 CI: [-9%, 67%], **Figure 3c**). Domination states of the microbiome increase the risk for BSIs in
150 immunocompromised cancer patients¹³; such dominations imply high relative abundances of single taxa,
151 and therefore a low diversity. Consistent with this, *Faecalibacterium* abundance was positively correlated
152 with diversity (R: 0.55, $p < 10^{-10}$, **Figure 3d**) in our data set and as reported previously³⁰.

153 We therefore next investigated a direct association between the bacteria populating the gut
154 microbiome and the organisms identified in the blood of patients. Visualizing the bacterial composition in
155 stool samples from patients alongside the BSI microorganism (**Supplementary Figure S4, Figure 3e**)
156 suggested a correspondence with the respective taxa identified in the blood: high abundances of the BSI-
157 causing microbes were found in corresponding stool samples (**Figure 3e**). To analyze this, we first
158 assigned stool samples associated with each BSI event into 5 categories defined by the taxonomic order
159 of the causative bacterial organisms, as well as one singleton group of a fungal infection case as a sixth

160 category; stool samples from uninfected patients were assigned a seventh, “uninfected” category. For
161 samples of each BSI category, we first calculated their median abundances of bacterial predictors in the
162 stool. We then ranked these stool taxon median abundances across BSI categories. As expected from
163 the visualization of sample compositions (**Figure 3e**), we found that BSI category sample sets were
164 generally enriched in their respective taxa in the stool. For example, samples associated with *Klebsiella*,
165 *Escherichia* or *Serratia* BSIs (Enbct category, **Figure 3f**) had the highest rank of Enterobacterales
166 abundances across the BSI category sample sets (**Figure 3f**). We tested this observation statistically
167 using the log₁₀-relative bacterial abundances in stool samples as independent predictors of identified BSI
168 pathogens, i.e. the BSI category, in a Bayesian categorical regression model where the uninfected class
169 was used as a pivot (see methods). In addition to taxon abundances, the model included the bacterial
170 α-diversity as a predictor. As expected, a strong statistical association between diversity and BSIs in
171 general was detected (**Supplementary Figure S5**). The rank analysis had suggested that
172 Staphylococcales are not enriched in BSIs by *Staphylococcus* (**Figure 3f**); this was supported by the
173 Bayesian model which showed that log₁₀-abundances of Staphylococcales in the stool were not
174 detectably predictive of a *Staphylococcus* BSI (**Figure 3g**). By contrast, our analysis demonstrated that
175 the bacterial abundances of all other BSI-causing organisms in the stool were predictive of corresponding
176 BSIs.

177 Collectively, these results reveal an unappreciated link between SARS-CoV-2 infection, gut
178 microbiome dysbiosis, and a major complication of COVID-19, BSIs. The loss of diversity and
179 immunosuppressive *Faecalibacterium* in patients with BSIs mirrored a similar loss of diversity and
180 Clostridiales in the mice receiving high doses of SARS-CoV-2, suggesting that this virus causally affects
181 the microbiome, either through direct infection^{35–39} or through a systemic inflammatory response^{2,4}.
182 However, the dysbiosis in patients with COVID-19 exceeded the microbiota shifts observed in the mouse
183 experiments, including microbiome dominations by single taxa, which was not seen in the mouse
184 experiments. It is possible that in our experiment, mice were sacrificed before perturbations to the gut
185 microbial populations reached a maximum. However, it is also plausible that the frequently administered
186 antibiotic treatments that hospitalized COVID-19 patients receive exacerbated SARS-CoV-2 induced
187 microbiome perturbations. Additionally, unlike the controlled environment experienced by laboratory mice,
188 hospitalized patients are uniquely exposed to antimicrobial-resistant infectious agents present on
189 surfaces and shed by other patients. Indeed, domination events where the gut is populated by only a few
190 taxa have been described in hospitalized, immunocompromised cancer patients treated with broad
191 spectrum antibiotics¹⁵. We frequently observed such dominations in our COVID-19 cohorts treated at two
192 hospitals.

193 Our observation that the type of bacteria that entered the bloodstream was disproportionately
194 enriched in the associated stool samples is a well characterized phenomenon in cancer patients¹³,
195 especially during chemotherapy induced leukocytopenia when patients are severely
196 immunocompromised^{11,30}. COVID-19 patients are also immunocompromised and frequently incur

197 lymphopenia, rendering them susceptible to secondary infections⁴⁰. Our data suggests dynamics in
198 COVID-19 patients may be similar to those observed in cancer patients: BSI-causing organisms may
199 translocate from the gut into the blood, potentially due to loss of gut barrier integrity, through virus-
200 induced tissue damage rather than chemotherapy. Consistent with this possibility, soluble immune
201 mediators such as TNF α and interferons produced during viral infections, including SARS-CoV-2,
202 damage the intestinal epithelium to disrupt the gut barrier, especially when the inflammatory response is
203 sustained as observed in patient with severe COVID-19^{41–43}.

204 One limitation of our data is temporal ordering of samples. Occasionally stool samples were
205 collected after observation of BSI, and this mismatch in temporal ordering is counter intuitive for gut-to-
206 blood translocation and a causal interpretation of our associations. However, the reverse direction, that
207 blood infection populates and changes the gut community, is unlikely for the organisms identified in the
208 blood, and if our associations were not causal, we would expect no match between BSI organisms and
209 stool compositions.

210 Taken together, our findings support a scenario in which gut-to-blood translocation of
211 microorganisms following microbiome dysbiosis, a known issue for chronic conditions such as cancer,
212 leads to dangerous BSIs during COVID-19. We suggest that investigating the underlying mechanism
213 behind our observations will inform the judicious application of antibiotics and immunosuppressives in
214 patients with respiratory viral infections and increase our resilience to pandemics.

215

216 **Materials and Methods**

217 *Bioethics statement*

218 The collection of COVID-19 human biospecimens for research has been approved by the NYUSOM
219 Institutional Review Board under il8-01121 Inflammatory Bowel Disease and Enteric Infection at NYU
220 Langone Health. The data presented in this study were also approved by Yale Human Research
221 Protection Program Institutional Review Boards (FWA00002571, protocol ID 2000027690). Informed
222 consent was obtained from all enrolled patients.

223

224 *Mouse experiments*

225 Cells & virus

226 Vero E6 (CRL-1586; American Type Culture Collection) were cultured Dulbecco's Modified Eagle's
227 Medium (DMEM, Corning) supplemented with 10% fetal bovine serum (FBS, Atlanta Biologics) and 1%
228 nonessential amino acids (NEAA, Corning). SARS-CoV-2, isolate USA-WA1/2020 19 (BEI resources
229 #NR52281), a gift from Dr. Mark Mulligan at the NYU Langone Vaccine Center was amplified once in
230 Vero E6 cells. All experiments with SARS-CoV-2 were conducted in the NYU Grossman School of
231 Medicine ABSL3 facility by personnel equipped with powered air-purifying respirators.

232

233 Mice

234 Heterozygous K18-hACE2 C57BL/6J mice (strain: 2B6.Cg-Tg(K18-ACE2)2PrImn/J) were obtained from
235 The Jackson Laboratory. Animals were housed in groups and fed standard chow diets. All animal studies
236 were performed according to protocols approved by the NYU School of Medicine Institutional Animal Care
237 and Use Committee (IACUC n°170209). 24-week-old K18-hACE2 males were administered either 10PFU
238 SARS-CoV-2 (low dose, LD), 10⁴PFU SARS-CoV-2 (high dose, HD) diluted in 50µL PBS (Corning) or
239 50µL PBS (non-infected, CTRL) via intranasal administration under xylazine-ketamine anesthesia
240 (AnaSedR AKORN Animal Health, Ketathesia™ Henry Schein Inc). Viral titer in the inoculum was
241 verified by plaque assay in Vero E6 cells. Following infection, mice were monitored daily for weight loss
242 and signs of disease. Stool samples were collected and stored at -80°C.

243

244 Measurement of viral load by plaque assay

245 Six or seven days after infection, mice were sacrificed. For some mice lungs were collected in Eppendorf
246 tubes containing 500µl of PBS and a 5mm stainless steel bead (Qiagen) and homogenized using with the
247 Qiagen TissueLyser II. Homogenates were cleared for 5 min at 5,000 × g, and viral supernatant was
248 frozen at -80°C for titration through plaque assay. In brief, Vero E6 cells were seeded at a density of 2.2 *
249 10⁵ cells per well in flat-bottom 24-well tissue culture plates. The following day, media was removed and
250 replaced with 100µL of tenfold serial dilutions of the virus stock, diluted in infection medium. Plates were
251 incubated for 1h at 37°C. Following incubation, cells were overlaid with 0.8% agarose in DMEM
252 containing 2% FBS and incubated at 37°C for 72hrs. Cells were then fixed with formalin buffered 10%
253 (Fisher Chemical) for 1h. Agarose plugs were then removed and cells were stained for 20 min with crystal
254 violet and then washed with tap water.

255

256 *Human study population and data collection*

257 This study involved 101 patients with laboratory-confirmed SARS-CoV-2 infection. SARS-CoV-2 infection
258 was confirmed by a positive result of real-time reverse transcriptase-polymerase chain reaction assay on
259 a nasopharyngeal swab. 64 patients were seen at NYU Langone Health, New York, for routine medical
260 procedures, outpatient care, or admitted through the Emergency Department at NYU Langone Health's
261 Tisch Hospital, New York City, between January 29, 2020 – July 2, 2020 and were followed until
262 discharge. In order to be eligible for inclusion in the study, stool specimens needed to be from individuals
263 >18 years of age. Data including demographic information, clinical outcomes, and laboratory results were
264 extracted from the electronic medical records in the NYU Langone Health clinical management system.
265 Blood and stool samples were collected by hospital staff. OmnigeneGut kits were used on collected stool.
266 In parallel, 37 patients were admitted to YNH with COVID-19 between 18 March 2020 and 27 May 2020
267 as part of the YALE IMPACT cohort described at length elsewhere². Briefly, participants were enrolled
268 after providing informed consent and paired blood and stool samples were collected longitudinally where
269 feasible for duration of hospital admission. No statistical methods were used to predetermine sample size

270 for this cohort. Demographic information of patients was aggregated through a systematic and
271 retrospective review of the EHR and was used to construct **Supplementary Table 3**. Symptom onset and
272 aetiology were recorded through standardized interviews with patients or patient surrogates upon
273 enrolment in our study, or alternatively through manual EHR review if no interview was possible owing to
274 clinical status at enrolment. The clinical data were collected using EPIC EHR and REDCap 9.3.6
275 software. At the time of sample acquisition and processing, investigators were blinded to patient clinical
276 status.

277

278 *DNA extraction and bacterial 16S rRNA sequencing*

279 For bacterial DNA extraction 700µL of SL1 lysis buffer (NucleoSpin Soil kit, Macherey-Nagel) was added
280 to the stool samples and tubes were heated at 95°C for 2h to inactivate SARS-CoV-2. Samples were then
281 homogenized using the FastPrep-24TM instrument (MP Biomedicals) and extraction was pursued using
282 the NucleoSpin Soil kit according to the manufacturer's instructions. DNA concentration was assessed
283 using a NanoDrop spectrophotometer. Samples with too low DNA concentration were excluded. DNA
284 from human samples was extracted with PowerSoil Pro (Qiagen) on the QiaCube HT (Qiagen), using
285 Powerbead Pro (Qiagen) plates with 0.5mm and 0.1mm ceramic beads. For mouse samples, the variable
286 region 4 (V4) of the 16S rRNA gene was amplified by PCR using primers containing adapters for MiSeq
287 sequencing and single-index barcodes. All PCR products were analyzed with the Agilent TapeStation for
288 quality control and then pooled equimolar and sequenced directly in the Illumina MiSeq platform using the
289 2x250 bp protocol. Human samples were prepared with a protocol derived from ⁴⁴, using KAPA HiFi
290 Polymerase to amplify the V4 region of the 16S rRNA gene. Libraries were sequenced on an Illumina
291 MiSeq using paired-end 2x250 reads and the MiSeq Reagent Kitv2.

292

293 *Bioinformatic processing and taxonomic assignment*

294 Amplicon sequence variants (ASVs) were generated via dada2 v1.16.0 using post-QC FASTQ files.
295 Within the workflow, the paired FASTQ reads were trimmed, and then filtered to remove reads containing
296 Ns, or with maximum expected errors ≥ 2 . The dada2 learn error rate model was used to estimate the
297 error profile prior to using the core dada2 algorithm for inferring the sample composition. Forward and
298 reverse reads were merged by overlapping sequence, and chimeras were removed before taxonomic
299 assignment. ASV taxonomy was assigned up to genus level using the SILVAv.138 database with the
300 method described in ⁴⁵ and a minimum bootstrapping support of 50%. Species-level taxonomy was
301 assigned to ASVs only with 100% identity and unambiguous matching to the reference.

302

303 *Compositional analyses*

304 α -Diversity

305 We calculated the inverse Simpson (*IVS*) index from relative ASV abundances (*p*) with *N* ASVs in a given

306 sample, $IVS = \frac{1}{\sum_i^N p_i^2}$.

307 Principal Coordinate Analyses

308 Bray-Curtis distances were calculated from the filtered ASV table using QIIME 1.9.1 and principal
309 components of the resulting distance matrix were calculated using the scikit-learn package for the Python
310 programming language, used to embed sample compositions in the first two principal coordinates (see
311 published code for the implementation in the Python programming language).

312

313 Average compositions and manipulation of compositions

314 To describe the average composition of a set of samples we calculated the central tendency of a
315 compositional sample⁴⁶. For counterfactual statistical analyses that require changes to a composition,
316 e.g. an increase in a specific taxon, we deployed the perturbation operation (\oplus), which is the
317 compositional analogue to addition in Euclidean space⁴⁶. A sample x containing the original relative taxon
318 abundances is perturbed by a vector y ,

319
$$y: x \oplus y = \left[\frac{x_1 y_1}{\sum_{i=1}^D x_i y_i}, \frac{x_2 y_2}{\sum_{i=1}^D x_i y_i}, \dots, \frac{x_D y_D}{\sum_{i=1}^D x_i y_i} \right] \forall x, y \in S^D$$

320 where S^D represents the D-part simplex.

321

322 *Statistical analyses*

323 Computer code alongside processed data tables are made available and can be used to reproduce the
324 statistical analysis and regenerate the figures (**Supplementary File 1**).

325

326 Bayesian t-test

327 To compare diversity measurements between different sample groups, e.g. different clinical status, we
328 performed a Bayesian estimation of group differences (BEST,⁴⁷), implemented using the pymc3 package
329 for the Python programming language; with priors (\sim) and deterministic calculations ($=$) to assess
330 differences in estimated group means as follows:

331 $g_1 \sim \text{Normal}(\mu = 15, \sigma = 15)$

332 $g_2 \sim \text{Normal}(\mu = 15, \sigma = 15)$

333 $\sigma_{g1} \sim \text{Uniform}(\text{low} = 1e-4, \text{high} = 30)$

334 $\sigma_{g2} \sim \text{Uniform}(\text{low} = 1e-4, \text{high} = 30)$

335 $v \sim \text{Exponential}(1/15) + 1$

336 $\lambda_1 = \sigma_{g1}^{-2}$

337 $\lambda_2 = \sigma_{g2}^{-2}$

338 $G1 \sim \text{StudentT}(\text{nu} = v, \text{mu} = g_1, \text{lam} = \lambda_1)$

339 $G2 \sim \text{StudentT}(\text{nu} = v, \text{mu} = g_2, \text{lam} = \lambda_2)$

340 $\Delta = G1 - G2$

341 Bayesian inference was performed using “No U-turn sampling”⁴⁸. Highest density intervals (HDI) of the
342 posterior estimation of group differences (Δ) were used to determine statistical certainty (***: 99% HDI >0

343 or <0, **: 95%HDI, *:90% HDI). The BEST code is provided in the Supplementary and implemented
344 following the pymc3 documentation (**Supplementary File 1**).

345

346 Bayesian logistic regression

347 We performed a Bayesian logistic regression to distinguish compositional differences between infection-
348 associated samples and samples from patients without secondary infections. We modeled the infection
349 state of patient sample i , y_i with a Binomial likelihood:

$$350 \quad y_i \sim \text{Binomial}(n = 1, p = p)$$

$$351 \quad p = \text{inverse logistic}(\alpha + X_i\beta)$$

$$352 \quad \alpha \sim \text{Normal}(\mu = 0, \sigma = 1)$$

$$353 \quad \beta \sim \text{Normal}(\mu = 0, \sigma = 1)$$

354 Where prior distributions are indicated by \sim ; α is the intercept of the generalized linear model, β is the
355 coefficient vector for the \log_{10} -relative taxon abundances X_i in sample i .

356

357 Bayesian categorical regression

358 To interrogate a correspondence between the taxon abundances in stool samples and the
359 microorganisms causing BSIs, we performed a Bayesian categorical regression. Briefly, we chose to
360 investigate an association between stool taxon abundances (independent predictor variable) and the
361 microbe identified in the blood (categorical outcome variable with seven unordered values) using a
362 multiclass regression (categorical regression). We estimated for each sample a probability of being
363 associated with one of the 6 BSI types (i.e. BSI by: Bacteroidaceae, Enterobacteriaceae,
364 Lactobacillaceae, Pseudomonadaceae, Staphylococcaceae, Saccharomycetaceae), and we used a
365 seventh class, uninfected, as a pivot. This means we are estimating a seven component simplicial vector
366 (s) containing the probabilities of a sample to be associated with one of the seven categories (6 BSI types
367 and uninfected). For each category, we set up a linear model (s_g , where g indicates the category). Each
368 linear model includes \log_{10} -relative stool taxon abundances of the taxa corresponding to the BSI category.
369 Furthermore, we had shown that alpha diversity (IVS) was globally associated with BSI; thus, diversity
370 was a predictor in each linear model. We set up a model using varying intercept and varying slope terms
371 such that the linear models used partially pooled coefficients for baseline risks ($\beta[1]$) and slopes
372 corresponding to the stool sample predictors ($\beta[2]$). The multiclass probabilities in s were then obtained
373 by applying the softmax function. The following model and priors were used:

$$374 \quad y_i \sim \text{Categorical}(p = p)$$

$$375 \quad p = \text{softmax}(s)$$

$$376 \quad z = (\sigma p * Lp) * zp$$

$$377 \quad s_{\text{Bacteroidaceae}} = \beta[1] + z[1,1] + (\beta[2] + z[2,1]) * X_{\text{Bacteroidaceae}} + \beta_{\text{diversity}} * \text{IVS}$$

$$378 \quad s_{\text{Enterobacteriaceae}} = \beta[1] + z[1,2] + (\beta[2] + z[2,2]) * X_{\text{Enterobacteriaceae}} + \beta_{\text{diversity}} * \text{IVS}$$

$$379 \quad s_{\text{Lactobacillaceae}} = \beta[1] + z[1,3] + (\beta[2] + z[2,3]) * X_{\text{Lactobacillaceae}} + \beta_{\text{diversity}} * \text{IVS}$$

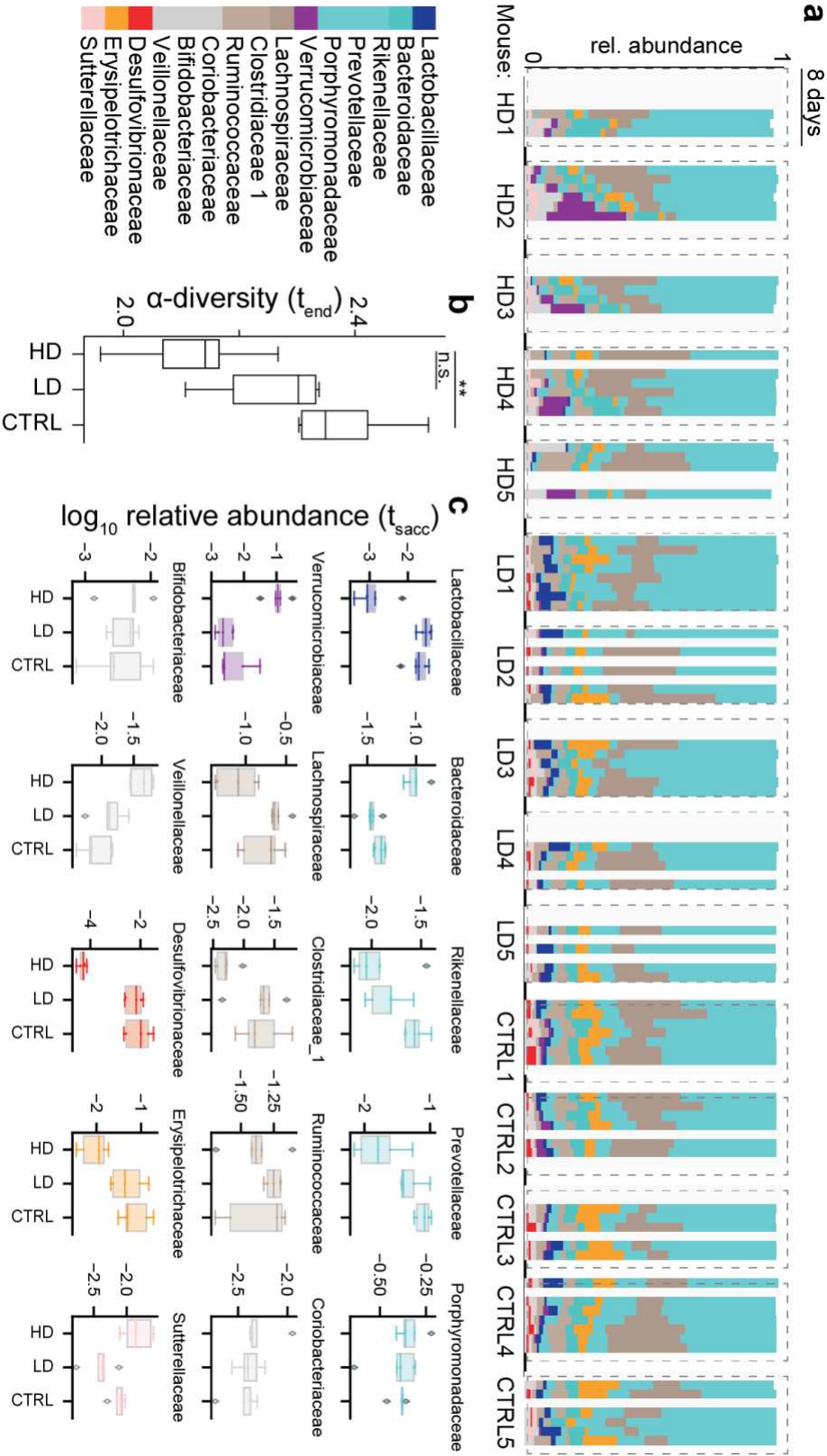
380 $S_{Pseudomonadaceae} = \beta[1] + z[1,4] + (\beta[2] + z[2,4]) * X_{Pseudomonadaceae} + \beta_{diversity} * IVS$
 381 $S_{Staphylococcaceae} = \alpha_{Staphylococcaceae} + \beta_{Staphylococcaceae} * X_{Staphylococcaceae} + \beta_{diversity} * IVS$
 382 $S_{Saccharomycetaceae} = \alpha_{Saccharomycetaceae} + \beta_{diversity} * IVS$
 383 $S_{uninfected} = 0$
 384 $\beta \sim \text{Normal}(\mu = 0, \sigma = 1)$
 385 $\sigma \sim \text{Exponential}(\lambda = 1)$
 386 $\sigma_p \sim \text{Exponential}(\lambda = 1)$
 387 $L_p \sim \text{LKJ_corr_choleski}(2)$
 388 $\alpha_{Staphylococcaceae} \sim \text{Normal}(\mu = 0, \sigma = 1)$
 389 $\beta_{Staphylococcaceae} \sim \text{Normal}(\mu = 0, \sigma = 1)$
 390 $\beta_{diversity} \sim \text{Normal}(\mu = 0, \sigma = 1)$
 391 $\alpha_{Saccharomycetaceae} \sim \text{Normal}(\mu = 0, \sigma = 2)$
 392 $z_p \sim \text{Normal}(\mu = 0, \sigma = 1)$

393
 394 Where p corresponds to the probabilities of each category, β is a two-component variable for the intercept
 395 and slope terms, representing the global baseline probability of bacterial infections with Bacteroidaceae,
 396 Enterobacteriaceae, Lactobacillaceae, and Pseudomonadaceae as well as the global slope coefficient for
 397 the effect of stool \log_{10} -relative abundances, which are partially pooling information across bacterial
 398 infection categories. To achieve partial pooling and account for correlations between varying intercepts
 399 and slopes (z), we jointly inferred the Choleski-factorized covariance matrix (σ , L_p , z_p), using the
 400 Lewandowski-Kurowicka-Joe (LKJ) distribution as a prior (LKJ_corr_choleski). $\beta_{diversity}$ is the coefficient for
 401 the effect of the *IVS* diversity. Of note, 16S rRNA sequencing does not provide abundances for the fungal
 402 infection by Saccharomycetaceae; therefore, we used only a baseline risk for this infection type
 403 ($\alpha_{Saccharomycetaceae}$) and *IVS* as predictors. To ensure equal prior probabilities for this category relative to the
 404 other categories, which have an additional predictor term and thus wider prior probabilities, we
 405 compensated the otherwise reduced prior uncertainty by widening the prior for $\alpha_{Saccharomycetaceae}$. Also, we
 406 assumed that infections by Staphylococcaceae could sometimes include contaminations from the skin of
 407 the patient or staff; therefore, we did not pool estimates for BSIs by Staphylococcaceae with other
 408 coefficients. The model was implemented in the STAN programming language and compiled using
 409 cmdstan. Code, the compiled STAN model, R notebooks to obtain and process the posterior chains, and
 410 data tables are provided in the supplement (**Supplementary File 2**).

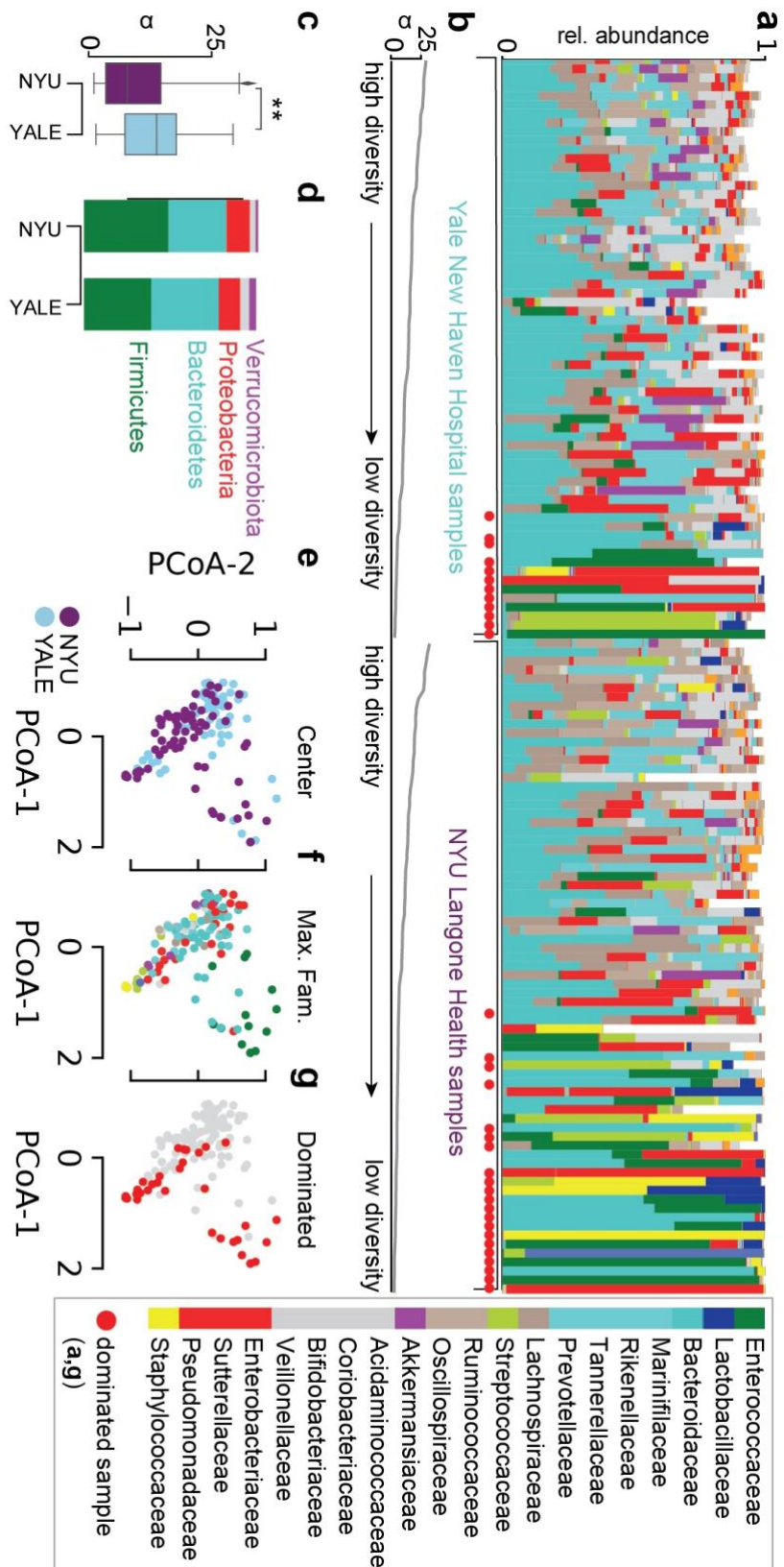
411

412 **Data Availability**

413 All data is made available as Supplementary. We provide code and data to reproduce the main analyses
414 in the form of jupyter notebooks and R notebooks, alongside processed “tidy” data tables, compiled STAN
415 programs and code to regenerate the figures. The raw sequencing data have been deposited on the
416 Sequencing Reads Archive (SRA), and SRA accession numbers are available for two bioprojects
417 corresponding to the mouse sequencing data (**Supplementary File 3**) and the human stool samples
418 (**Supplementary File 4**).



421 **Figure 1. SARS-CoV-2 infection causes gut microbiome alterations in mice.** **a** Timelines of fecal
422 microbiota composition measured by 16S rRNA gene sequencing in mice infected with high (HD,
423 10^4 PFU), or low doses (LD, 10PFU) and in uninfected control mice (CTRL); time of infection=Day 1. Bars
424 represent the composition of the 30 most abundant bacterial families per sample, blocks of samples
425 correspond to an individual mouse's time course. **b** α -diversity (Shannon) in the final samples per
426 infection group; **: HDI95<0 BEST. **c** \log_{10} -relative family abundances at the final time point. heavy
427 breathing, reduced activity and hunched posture (Supplementary Table S1).



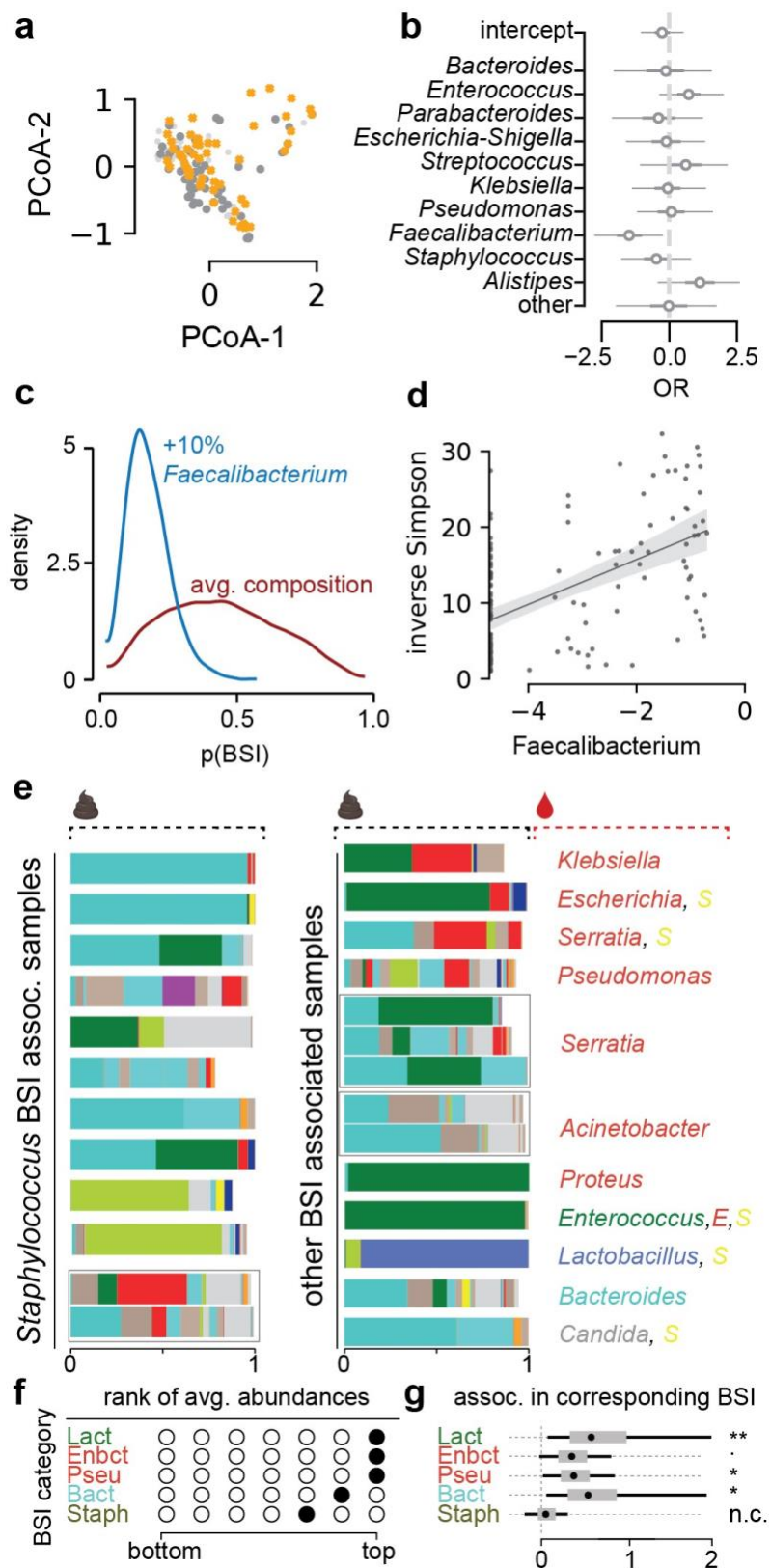
428

429

430

Figure 2. Gut microbiome bacterial compositions during COVID-19 in patients from NYU Langone Health and Yale New Haven Hospital. a Bacterial family composition in stool samples identified by 16S

431 rRNA gene sequencing; bars represent the relative abundances of bacterial families; red circles indicate
432 samples with single taxa >50%. Samples are sorted by the bacterial α -diversity (inverse Simpson index,
433 **b**). **c** α -diversity in samples from NYU Langone Health and Yale New Haven Hospital. **d** Average phylum
434 level composition per center. **e-g** Principal coordinate plots of all samples shown in **a**, labeled by center
435 (**e**), most abundant bacterial family (**f**) and domination status of the sample (**g**).
436
437
438



439

440

441

Figure 3. Microbiome composition is associated with secondary bloodstream infections. **a** Principal coordinate plot of all samples, BSI associated samples in orange. **b** Posterior coefficient estimates from a

442 Bayesian logistic regression regressing \log_{10} relative abundances of the top 10 most abundant bacterial
443 genera on BSI status. **c** Posterior prediction of BSI risk based on bacterial composition contrasting the
444 predicted risk of the average composition across all samples (red) with the risk estimated for the same
445 composition changed such that *Faecalibacterium* was increased by 10% (blue). **d** \log_{10} relative
446 abundances of *Faecalibacterium* correlated with α -diversity, shaded region: 95%CI. **e** Sample
447 compositions with BSIs indicated; left: *Staphylococcus* BSI associated samples; right: other BSI associated
448 samples, the BSI causing microbial genus annotated in colors corresponding to the colors in stool
449 microbiome compositions. **f** Rank analysis of abundance patterns in stool samples from different BSI
450 categories; a filled circle indicates the calculated rank of the focal BSI category (row) in terms of the
451 corresponding taxon stool abundance relative to samples from other BSI categories (only 5 out of 7 BSI
452 categories are shown because fungal BSIs and the uninfected category have no corresponding bacterial
453 stool abundances). **g** Posterior coefficients of the statistical association between bacterial order \log_{10}
454 relative abundances of BSI causing bacteria and BSI events from a hierarchical Bayesian categorical
455 regression; **: 95%HDI>0, *: 90%HDI>0, .:85% HDI>0.
456

457 **Acknowledgments**

458 We thank René Niehus for helpful discussions on the implementation of the various Bayesian analyses.
459 We thank the NYU Langone's Genome Technology Center supported in part by NYU Langone Health's
460 Laura and Isaac Perlmutter Cancer Center Support (grant P30CA016087) from the National Cancer
461 Institute Langone for the mouse gut microbiota 16S rRNA sequencing.

462

463 **Yale IMPACT Team**

464 Abeer Obaid, Alice Lu-Culligan, Allison Nelson, Anderson Brito, Angela Nunez, Anjelica Martin, Annie
465 Watkins, Bertie Geng, Chaney Kalinich, Christina Harden, Codruta Todeasa, Cole Jensen, Daniel Kim,
466 David McDonald, Denise Shepard, Edward Courchaine, Elizabeth B. White, Eric Song, Erin Silva, Eriko
467 Kudo, Giuseppe Deluliis, Harold Rahming, Hong-Jai Park, Irene Matos, Jessica Nouws, Jordan Valdez,
468 Joseph Fauver, Joseph Lim, Kadi-Ann Rose, Kelly Anastasio, Kristina Brower, Laura Glick, Lokesh
469 Sharma, Lorenzo Sewanan, Lynda Knaggs, Maksym Minasyan, Maria Batsu, Mary Petrone, Maxine
470 Kuang, Maura Nakahata, Melissa Campbell, Melissa Linehan, Michael H. Askenase, Michael Simonov,
471 Mikhail Smolgovsky, Nicole Sonnert, Nida Naushad, Pavithra Vijayakumar, Rick Martinello, Rupak Datta,
472 Ryan Handoko, Santos Bermejo, Sarah Prophet, Sean Bickerton, Sofia Velazquez, Tara Alpert, Tyler
473 Rice, William Khoury-Hanold, Xiaohua Peng, Yexin Yang, Yiyun Cao & Yvette Strong

474

475 **Author contributions**

476 LBR performed the mouse experiments with help from MGN, AMVJ. MV, JEA and JS prepared the
477 samples from NYU. MV, JEA prepared the clinical data from NYU with help from JG, EW, BS. JK
478 provided the data from Yale with help from ACM and the IMPACT team, AIK and AI. JS designed and
479 performed the analyses with help from GAH and APS. JS and KC designed the research question with
480 support from VJT and BS. JS and KC wrote the manuscript. All other authors contributed materials,
481 scientific feedback and commented on the manuscript.

482

483 **Funding**

484 This work was in part funded by NYU Grossman School of Medicine startup research funds to JS, and the
485 Yale School of Public Health and the Beatrice Kleinberg Neuwirth Fund, as well as NIH grants to KC
486 (DK093668, AI121244, HL123340, AI130945, AI140754, DK124336), a Faculty Scholar grant from the
487 Howard Hughes Medical Institute (KC), Crohn's & Colitis Foundation (KC), Kenneth Rainin Foundation
488 (KC), Judith & Stewart Colton Center of Autoimmunity (KC). Further funding was provided by grants from
489 the NIH/NIAID to MD (R01AI143639 and R21AI139374), by Jan Vilcek/David Goldfarb Fellowship
490 Endowment Funds to AMVJ, by The G. Harold and Leila Y. Mathers Charitable Foundation to MD, and by
491 NYU Grossman School of Medicine Startup funds to MD and KAS, and the NYU Grossman School of
492 Medicine COVID-19 seed research funds to VJT. MN was supported by the American Heart Association
493 Postdoctoral Fellowship 19-A0-00-1003686. IMPACT received support from the Yale COVID-19

494 Research Resource Fund. AI and DRL are Investigators of the Howard Hughes Medical Institute. AIK
495 received support from the Beatrice Kleinberg Neuwirth Fund, Bristol Meyers Squibb Foundation and
496 COVID-19 research funds from the Yale Schools of Public Health and Medicine.

497

498 **Conflicts**

499 KC has received research support from Pfizer, Takeda, Pacific Biosciences, Genentech, and Abbvie;
500 consulted for or received an honoraria from Puretech Health, Genentech, and Abbvie; and holds U.S.
501 patent 10,722,600 and provisional patents 62/935,035 and 63/157,225. JS is cofounder of Postbiotics
502 Plus Research LLC.

503

504 **Bibliography**

- 505
506 1. Fajgenbaum, D. C. & June, C. H. Cytokine Storm. *N. Engl. J. Med.* **383**, 2255–2273 (2020).
507 2. Lucas, C. *et al.* Longitudinal analyses reveal immunological misfiring in severe COVID-19. *Nature*
508 **584**, 463–469 (2020).
509 3. Zuo, T. *et al.* Alterations in Gut Microbiota of Patients With COVID-19 During Time of Hospitalization.
510 *Gastroenterology* **159**, 944–955.e8 (2020).
511 4. Yeoh, Y. K. *et al.* Gut microbiota composition reflects disease severity and dysfunctional immune
512 responses in patients with COVID-19. *Gut* **70**, 698–706 (2021).
513 5. Nori, P. *et al.* Bacterial and fungal coinfections in COVID-19 patients hospitalized during the New
514 York City pandemic surge. *Infect. Control Hosp. Epidemiol.* **42**, 84–88 (2021).
515 6. Grasselli, G. *et al.* Hospital-Acquired Infections in Critically Ill Patients With COVID-19. *Chest* (2021).
516 doi:10.1016/j.chest.2021.04.002
517 7. Langford, B. J. *et al.* Bacterial co-infection and secondary infection in patients with COVID-19: a
518 living rapid review and meta-analysis. *Clin. Microbiol. Infect.* **26**, 1622–1629 (2020).
519 8. Buffie, C. G. *et al.* Precision microbiome reconstitution restores bile acid mediated resistance to
520 *Clostridium difficile*. *Nature* **517**, 205–208 (2015).
521 9. Buffie, C. G. & Pamer, E. G. Microbiota-mediated colonization resistance against intestinal
522 pathogens. *Nat. Rev. Immunol.* **13**, 790–801 (2013).
523 10. Modi, S. R., Collins, J. J. & Relman, D. A. Antibiotics and the gut microbiota. *J. Clin. Invest.* **124**,
524 4212–4218 (2014).
525 11. Morjaria, S. *et al.* Antibiotic-Induced Shifts in Fecal Microbiota Density and Composition during
526 Hematopoietic Stem Cell Transplantation. *Infect. Immun.* **87**, (2019).
527 12. Niehus, R. *et al.* Quantifying antibiotic impact on within-patient dynamics of extended-spectrum beta-
528 lactamase resistance. *Elife* **9**, (2020).
529 13. Taur, Y. *et al.* Intestinal domination and the risk of bacteremia in patients undergoing allogeneic
530 hematopoietic stem cell transplantation. *Clin. Infect. Dis.* **55**, 905–914 (2012).
531 14. Taur, Y. *et al.* Reconstitution of the gut microbiota of antibiotic-treated patients by autologous fecal
532 microbiota transplant. *Sci. Transl. Med.* **10**, (2018).
533 15. Liao, C. *et al.* Compilation of longitudinal microbiota data and hospitalome from hematopoietic cell
534 transplantation patients. *Sci. Data* **8**, 71 (2021).
535 16. Peled, J. U. *et al.* Microbiota as Predictor of Mortality in Allogeneic Hematopoietic-Cell
536 Transplantation. *N. Engl. J. Med.* **382**, 822–834 (2020).
537 17. Yu, D. *et al.* Low prevalence of bloodstream infection and high blood culture contamination rates in
538 patients with COVID-19. *PLoS One* **15**, e0242533 (2020).
539 18. Wang, D. *et al.* Clinical Characteristics of 138 Hospitalized Patients With 2019 Novel Coronavirus-
540 Infected Pneumonia in Wuhan, China. *JAMA* **323**, 1061–1069 (2020).
541 19. Westblade, L. F., Simon, M. S. & Satlin, M. J. Bacterial coinfections in coronavirus disease 2019.
542 *Trends Microbiol.* (2021). doi:10.1016/j.tim.2021.03.018
543 20. Sepulveda, J. *et al.* Bacteremia and Blood Culture Utilization during COVID-19 Surge in New York
544 City. *J. Clin. Microbiol.* **58**, (2020).
545 21. Lansbury, L., Lim, B., Baskaran, V. & Lim, W. S. Co-infections in people with COVID-19: a
546 systematic review and meta-analysis. *J. Infect.* **81**, 266–275 (2020).
547 22. Sieswerda, E. *et al.* Recommendations for antibacterial therapy in adults with COVID-19 - an
548 evidence based guideline. *Clin. Microbiol. Infect.* **27**, 61–66 (2021).
549 23. Zhai, B. *et al.* High-resolution mycobiota analysis reveals dynamic intestinal translocation preceding
550 invasive candidiasis. *Nat. Med.* **26**, 59–64 (2020).
551 24. Haak, B. W. *et al.* Impact of gut colonization with butyrate-producing microbiota on respiratory viral
552 infection following allo-HCT. *Blood* **131**, 2978–2986 (2018).
553 25. Steed, A. L. *et al.* The microbial metabolite desaminotyrosine protects from influenza through type I
554 interferon. *Science* **357**, 498–502 (2017).
555 26. Abt, M. C. *et al.* Commensal bacteria calibrate the activation threshold of innate antiviral immunity.
556 *Immunity* **37**, 158–170 (2012).
557 27. Ichinohe, T. *et al.* Microbiota regulates immune defense against respiratory tract influenza A virus
558 infection. *Proc. Natl. Acad. Sci. USA* **108**, 5354–5359 (2011).

- 559 28. Sencio, V. *et al.* Influenza infection impairs the gut's barrier properties and favors secondary enteric
560 bacterial infection through reduced production of short-chain fatty acids. *Infect. Immun.* (2021).
561 doi:10.1128/IAI.00734-20
- 562 29. Wang, J. *et al.* Respiratory influenza virus infection induces intestinal immune injury via microbiota-
563 mediated Th17 cell-dependent inflammation. *J. Exp. Med.* **211**, 2397–2410 (2014).
- 564 30. Schluter, J. *et al.* The gut microbiota is associated with immune cell dynamics in humans. *Nature*
565 **588**, 303–307 (2020).
- 566 31. Gopalakrishnan, V. *et al.* Gut microbiome modulates response to anti-PD-1 immunotherapy in
567 melanoma patients. *Science* **359**, 97–103 (2018).
- 568 32. Diefenbach, C. S. *et al.* Microbial dysbiosis is associated with aggressive histology and adverse
569 clinical outcome in B-cell non-Hodgkin lymphoma. *Blood Adv.* **5**, 1194–1198 (2021).
- 570 33. Sokol, H. *et al.* Faecalibacterium prausnitzii is an anti-inflammatory commensal bacterium identified
571 by gut microbiota analysis of Crohn disease patients. *Proc. Natl. Acad. Sci. USA* **105**, 16731–16736
572 (2008).
- 573 34. Wrzosek, L. *et al.* Bacteroides thetaiotaomicron and Faecalibacterium prausnitzii influence the
574 production of mucus glycans and the development of goblet cells in the colonic epithelium of a
575 gnotobiotic model rodent. *BMC Biol.* **11**, 61 (2013).
- 576 35. Gaebler, C. *et al.* Evolution of antibody immunity to SARS-CoV-2. *Nature* **591**, 639–644 (2021).
- 577 36. Park, S.-K. *et al.* Detection of SARS-CoV-2 in Fecal Samples From Patients With Asymptomatic and
578 Mild COVID-19 in Korea. *Clin. Gastroenterol. Hepatol.* **19**, 1387–1394.e2 (2021).
- 579 37. Xiao, F. *et al.* Evidence for Gastrointestinal Infection of SARS-CoV-2. *Gastroenterology* **158**, 1831–
580 1833.e3 (2020).
- 581 38. Cheung, K. S. *et al.* Gastrointestinal Manifestations of SARS-CoV-2 Infection and Virus Load in
582 Fecal Samples From a Hong Kong Cohort: Systematic Review and Meta-analysis. *Gastroenterology*
583 **159**, 81–95 (2020).
- 584 39. Lamers, M. M. *et al.* SARS-CoV-2 productively infects human gut enterocytes. *Science* **369**, 50–54
585 (2020).
- 586 40. Wang, L. *et al.* An observational cohort study of bacterial co-infection and implications for empirical
587 antibiotic therapy in patients presenting with COVID-19 to hospitals in North West London. *J.*
588 *Antimicrob. Chemother.* **76**, 796–803 (2021).
- 589 41. Matsuzawa-Ishimoto, Y. *et al.* Autophagy protein ATG16L1 prevents necroptosis in the intestinal
590 epithelium. *J. Exp. Med.* **214**, 3687–3705 (2017).
- 591 42. Labarta-Bajo, L. *et al.* Type I IFNs and CD8 T cells increase intestinal barrier permeability after
592 chronic viral infection. *J. Exp. Med.* **217**, (2020).
- 593 43. Karki, R. *et al.* Synergism of TNF- α and IFN- γ Triggers Inflammatory Cell Death, Tissue Damage,
594 and Mortality in SARS-CoV-2 Infection and Cytokine Shock Syndromes. *Cell* **184**, 149–168.e17
595 (2021).
- 596 44. Gohl, D. M. *et al.* Systematic improvement of amplicon marker gene methods for increased accuracy
597 in microbiome studies. *Nat. Biotechnol.* **34**, 942–949 (2016).
- 598 45. Wang, Q., Garrity, G. M., Tiedje, J. M. & Cole, J. R. Naive Bayesian classifier for rapid assignment of
599 rRNA sequences into the new bacterial taxonomy. *Appl. Environ. Microbiol.* **73**, 5261–5267 (2007).
- 600 46. Pawlowsky-Glahn, V., Egozcue, J. J. & Tolosana-Delgado, R. *Modelling and analysis of*
601 *compositional data.* (John Wiley & Sons, Ltd, 2015). doi:10.1002/9781119003144
- 602 47. Kruschke, J. K. Bayesian estimation supersedes the t test. *J. Exp. Psychol. Gen.* **142**, 573–603
603 (2013).
- 604 48. Homan, M. D. & Gelman, A. The No-U-Turn Sampler: Adaptively Setting Path Lengths in
605 Hamiltonian Monte Carlo. *J. Mach. Learn. Res.* **15**, 1593–1623 (2014).
- 606

Supplementary Files

This is a list of supplementary files associated with this preprint. Click to download.

- [supplementarydatafile.pdf](#)